Rayleigh-Taylor instability with complex acceleration history

Guy Dimonte,[1] Praveen Ramaprabhu,[1,2] and Malcolm Andrews[1]
[1]*Los Alamos National Laboratory, Los Alamos, New Mexico 87545, USA*
[2]*University North Carolina at Charlotte, Charlotte, North Carolina 28233, USA*
(Received 2 July 2007; published 23 October 2007)

Experiments and numerical simulations are performed on the Rayleigh-Taylor instability with a complex acceleration history $g(t)$ consisting of consecutive periods of acceleration, deceleration, and acceleration. The dominant bubbles and spikes that grow in the initial unstable phase are found to be shredded by the trailing structures during the stable deceleration phase. This reduces their diameter at the front and increases the atomic mixing such that the growth during the final unstable acceleration is retarded. The simulations are able to describe the bubble evolution only if broadband initial perturbations are assumed. Such a complex $g(t)$ is useful for validating mix models.

DOI: 10.1103/PhysRevE.76.046313 PACS number(s): 47.20.Bp

I. INTRODUCTION

The Rayleigh-Taylor (RT) instability occurs when a fluid of density ρ_H is accelerated or supported against gravity by a fluid of lower density ρ_L. It affects phenomena from inertial confinement fusion (ICF) [1] to supernova explosions [2] in the regime of large Reynolds number (Re). Three-dimensional (3D) numerical simulations (NS) can fully resolve the instability for $\mathrm{Re} \leqslant 10^5$ when the flow involves simple hydrodynamics. This becomes more difficult in simulating ICF and supernovas because computational power must be used to describe a wide variety of ancillary physics. Fortunately, for $\mathrm{Re} \gg 1$, the instability is broadband and evolves self-similarly so that it can be described using turbulence models with realistic resolution.

Turbulent mix models are phenomenological and thus require validation under different temporal acceleration histories $g(t)$ [3,4]. For example, when g is constant, the light fluid penetrates the heavy fluid as bubbles with amplitude $h_b = \alpha_b\ Agt^2$ where $A \equiv (\rho_H - \rho_L)/(\rho_H + \rho_L)$ is the Atwood number. Experiments [3,5–8] and NS [9–13] obtain $\alpha_b \sim 0.02-0.07$ where the variance may by due to the initial conditions [13,14]. When the acceleration is impulsive, the bubble amplitude increases as $h_b \propto t^{0.25\pm0.05}$ for all A [7,9,10]. However, these relatively simple flows can be described successfully by many models including buoyancy-drag models [15–18], turbulent diffusion models [19–21], and multiphase models [6,22,23]. A full evaluation of mix models requires more complex acceleration histories as discussed by Llor [4]. Reversals in g are particularly useful because they may involve demixing [24,25].

In this paper, we investigate the RT instability with a complex acceleration history consisting of consecutive periods of acceleration, deceleration, and acceleration. Experiments on the Linear Electric Motor [3] (LEM) are compared with the incompressible, 3D code RTI-3D [11,26]. We find that the dominant bubbles and spikes produced during the initial acceleration reverse their flow during the deceleration period and are shredded as they encounter chaotic trailing structures. This causes the size of the dominant structures at the front of the mixing zone to decrease by ~50% and the atomic mixing to increase to ~100%. As a result, the growth during the final unstable acceleration is retarded. The NS are performed with two limiting initial spectra, one with only short wavelengths [6,9,11,12] that promotes bubble merger and another with a broadband spectrum that promotes bubble competition [13,14]. Good agreement is obtained with the experiments, but only when initialized with broadband perturbations.

II. EXPERIMENTAL AND NUMERICAL TECHNIQUES

The experiments are conducted on the LEM [3,7] with the measured acceleration history shown in Fig. 1(a) scaled to Earth's gravity g_0. The two RT-unstable acceleration stages are generated by independently triggered capacitor banks at different times. The intermediate RT-stable deceleration stage is produced with a mechanical leaf-spring brake. The transitions are gradual due to the rise and fall times of the circuits and the gradual engagement and disengagement of the brake by the cell. The velocity (dotted line) in Fig. 1(b) is obtained by integrating $g(t)$ in time. The impulse from the first acceleration is adjusted to be nearly equal to that applied

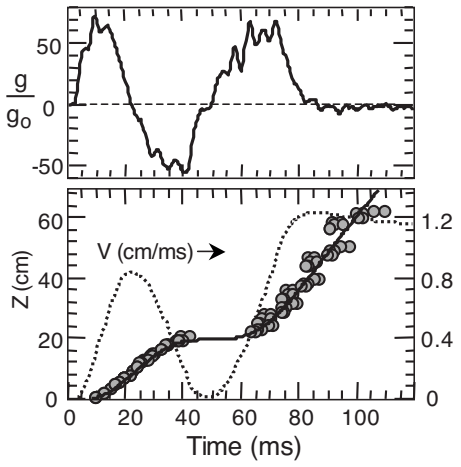

FIG. 1. (a) Scaled acceleration and (b) velocity and displacement vs time. Lines from measured acceleration and points measured directly.

by the brake so that the cell is nearly stopped. The calculated displacement $Z=\int dt' \int dt'' g(t'')$ (solid line) in Fig. 1(b) is in good agreement with the points measured with laser position detectors [7]. The reproducibility is excellent during the first acceleration period because the drive is electrical. The mechanical braking is less reproducible because the leaf springs fatigue with use. This increases the scatter in the data late in time.

The fluids are hexane ($\rho_L=0.66$ g/cm^3) and water salted with NaI ($\rho_H=1.87$ g/cm^3) because they are transparent and have a moderate $A=0.48$. The surface tension was measured to be $\sigma\sim 8$ dyn/cm (fill No. 31 in Ref. [7]). Liquid combinations with smaller A are better diagnosed with lasers, but the RT growth is weaker over the limited duration of each stage. The growth is largest with a liquid-gas combination at $A\sim 1$, but the deceleration stage is compromised by surface tension.

The numerical simulations are perfomed with a 3D incompressible Eulerian code RTI-3D [11,26] using the measured $g(t)$. The code uses operator splitting with projection and third-order-accurate Van Leer advection limiters. Volume fractions f_L and f_H are used to mark the light and heavy fluids. Then, a multigrid Poisson solver calculates the pressure correction field. We use an incompressible, code because the experiment is incompressible, but compressible codes could also be applicable.

The NS are initialized with two limiting interfacial perturbation spectra—namely, one that promotes bubble merger and another for bubble competition. In the early simulations, Youngs [6,9] used only short-wavelength initial perturbations to compensate for the relatively low resolution (numerical Reynolds number) because they grow relatively fast and couple nonlinearly to produce longer-wavelength modes by the merger process. This quickly approaches the self-similar evolution of a high-Reynolds-number flow and produces a universal lower bound on α_b. For this reason, such an annular (An) wave number spectrum was chosen in the Alpha-group comparative study [11], which obtained $\alpha_b \sim 0.02-0.03$ from a wide variety of codes. However, since experiments exceed this lower bound, it was thought (Refs. [13,14] and references therein) that their initial perturbations were more broadband (Bb) and grew via the amplification and saturation of seeded modes—namely, by bubble competition. NS [13] with a Bb initial spectra were able to reproduce experimental results by adjusting the initial amplitude whereas those with the An spectrum obtained the same lower bound as in Refs. [11,12] independent of amplitude.

The initial spectral types have the following characterisitcs. The annular (An) wave number spectrum promoting bubble merger uses a constant envelope between modes 32 and 64. The broadband (Bb) spectrum promoting bubble competition uses an envelope that varies as k^{-2} between modes 3 and 64. Within each envelope, the amplitudes and phases are chosen randomly and the scaled root-mean-squared (rms) initial amplitude $k\langle h_0\rangle$ is integrated over the range $k_0(1\pm 3/8)$ centered at the most linearly unstable mode k_0 [14]. In previous studies [13,14], α_b is found to be insensitive to $k\langle h_0\rangle$ for the An spectrum due to the strong nonlinearities whereas it increases grows logarithmically with $k\langle h_0\rangle$ for the Bb spectrum.

The experiments and NS are compared quantitatively using several metrics. The bubble and spike amplitudes are obtained in the experiment from backlit images as described in Ref. [7]. The backlighters consist of xenon flash lamps of 5 μs duration to freeze the motion and they are triggered at specific locations by the laser-based detectors. The NS obtain h_b and h_s from the 1% and 99% levels of the spanwise-averaged volume fraction. We also compare the diameter of the dominant bubbles and spikes at the fronts of the mixing zone, D_b and D_s, because they affect the dynamics [14]. They are measured using the autocorrelation function of the bubble and spike profiles [7,11,13]. In the experiments, the profiles are obtained in 1D by applying edge detection techniques to backlit images. In the NS, we use the 2D profiles of the contours where $f_L=1\%$ and 99%. By analyzing test images with objects of known sizes, it was found [7] that their average radius is given approximately by the displacement that reduces the autocorrelation function to 30%.

III. RESULTS

Sample experimental images (left column) and 2D slices of volume fraction from the NS are shown in Fig. 2. The positive acceleration is downward in order to produce the instability since the fluids are prepared in Earth's gravity with the light fluid on top. The cell is 3D with a 7.3-cm-square horizontal cross section and a 8.7 cm height, but the images are cropped in Z for brevity. In the first image, we superimpose the profiles of the bubble (bottom) and spike (top) fronts, offset in Z for clarity. They are used to determine D_b and D_s as described in Sec. II. The false color images in the central and rightmost columns are volume fraction slices from the NS with the Bb and An spectra. In the first two rows, the bubbles and spikes grow self-similarly in size and amplitude. They reverse direction during the strong deceleration (third row) and collide with the trailing structures. This produces horizontal bands of fully mixed fluids in the NS. In the LEM experiments, surface tension inhibits atomic mixing, but it does allow small droplets to form of order $D_b\sim \pi/k_0\sim \pi(3\sigma/\delta\rho g)^{1/2}\sim 0.05$ cm, consistent with Fig. 2(c). Then, bubbles and spikes resume their self-similar growth during the final acceleration period (fourth row).

The cell acceleration, bubble amplitude, and aspect ratio D_b/h_b are plotted versus the displacement Z in Figs. 3(a)–3(c). The points are measured and the colored lines represent the NS described below. For $Z\leqslant 8.5$ cm, the acceleration is positive and the amplitudes grow with an initial slope $\alpha_b\equiv(dh_b/dZ)/2A\sim 0.1$. Such large values of α_b can occur [11–13] because the initial perturbations have $h_b\ll D_b$ [as seen in Fig. 3(c)], and their growth is exponential initially according to linear theory. Near $Z=6$ cm, the amplitudes become nonlinear since $h_b\sim D_b$ and the growth becomes self-similar with ($D_b\propto h_b$) and α_b decreases to a more asymptotic value.

The buoyancy force is reversed for 8.5 cm$<Z<$20 cm, causing the amplitude h_b and aspect ratio D_b/h_b to decrease by 20% and 50%, respectively. By studying images such as Fig. 2(c), we propose the following scenario. Typically, the largest bubbles in a mixing layer are at the front because they

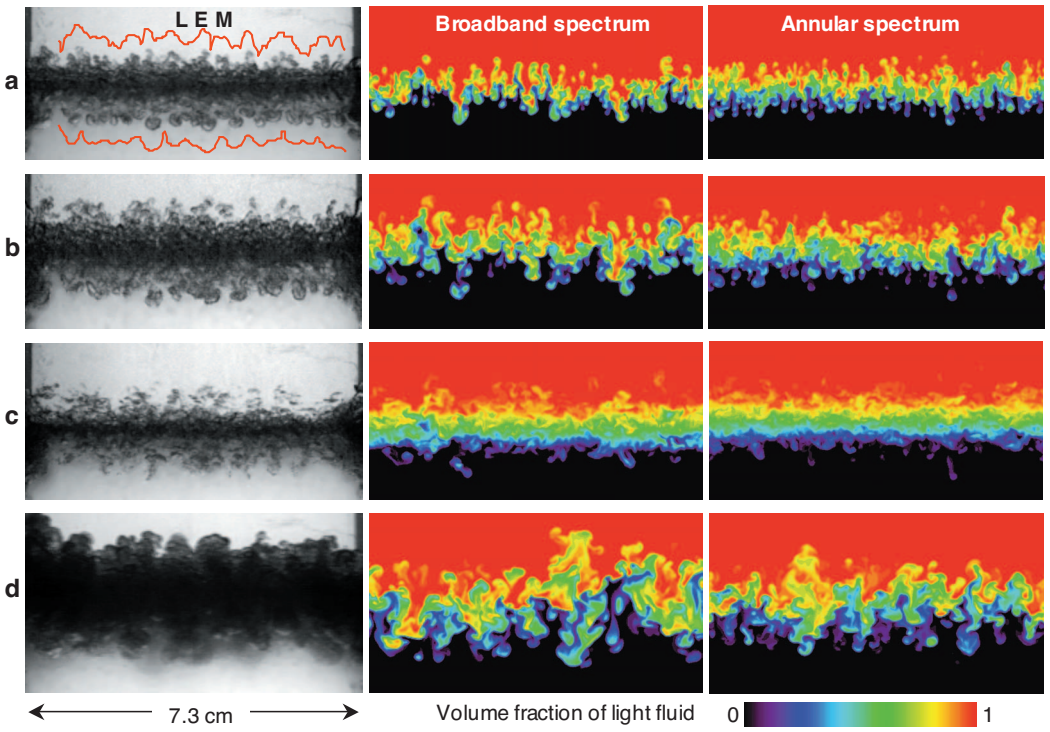

FIG. 2. (Color) Backlit images from LEM (left column) and volume fraction from NS for Bb (middle column) and An (right column) initial spectra at different times (locations) (a) 19.6 (7), (b) 26.8 (13), (c) 34.4 (18.4), and (d) 65.2(25.4) ms (cm).

experience the smallest drag force and they are trailed by smaller structures with more drag. When buoyancy is reversed, the dominant bubbles at the front collide with the trailing less mobile structures thereby shreding them into small fragments as seen in Fig. 2(c). By analyzing the edge profile [7], we find that D_b/h_b decreases from 40% to 20% during the deceleration as seen in Fig. 3(c). This scenario suggests that the contraction in the turbulent mixing zone should be of order $\delta h_b \propto D_b$ during the deceleration stage.

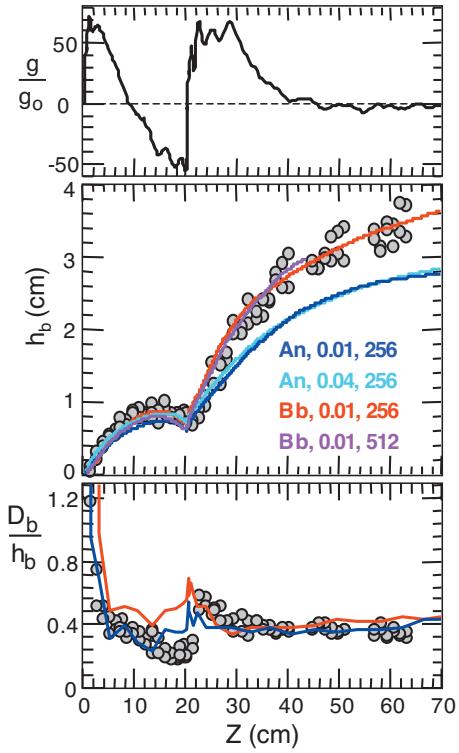

FIG. 3. (Color) Acceleration, and amplitude and aspect ratio for bubbles vs displacement. Points and g are measured and lines are from NS with different spectra, $\langle kh_0 \rangle$, and zoning.

For 20 cm$<Z<$40 cm, the cell is reaccelerated and the RT instability resumes growing in a complex way. There is a short delay (~2 cm) before the the amplitude resumes growing possibly because D_b is relatively small and the atomic mixing is high (see the NS below). Then, h_b grows with a very large slope $\alpha_b \sim 0.15$ while the aspect ratio jumps to $D_b/h_b \sim 0.6$ and then decays to the asymptotic value ~0.35. For $Z>40$ cm, the cell decelerates slightly due to the mechanical supports and the RT growth rate decays.

The spike evolution is similar to that of bubbles, as shown in Fig. 4, but the magnitudes differ because $A \sim 0.48$. Generally, the spike amplitude h_s is 20%–30% larger than h_b and the aspect ratio D_s/h_s is 75% smaller than D_b/h_b. The temporal evolution has the same characteristics seen in Fig. 3. The amplitude saturates and decreases 20% during the deceleration and grows vigorously during the reacceleration. Similalry, the aspect ratio decreases during the deceleration, then jumps initially upon reacceleration, and decays to a more asymptotic level in the end.

Many NS have been performed, but only four results are shown here to exemplify the sensitivity to zoning and initial wave number (k) spectrum. The NS with the Bb spectrum compare more favorably with the experiments than those with the An spectrum. For the bubbles, the Bbspectrum is fit to the data by choosing $k\langle h_0 \rangle = 0.01$. The agreement is good for the entire duration and independent of the zoning of

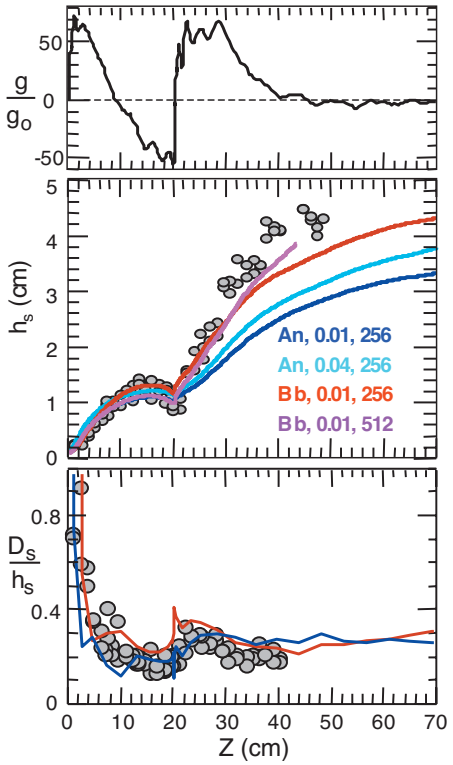

FIG. 4. (Color) Acceleration and amplitude and aspect ratio for spikes vs displacement. Points and g are measured and lines are from NS with different spectra, $\langle kh_0\rangle$, and zoning.

$512\times512\times512$ (purple) and $256\times256\times512$ (red). Since the NS appear to be converged, we used a zoning of $256\times256\times512$ for the An spectra. Here, there is good agreement with data only in the first two stages even when the initial amplitude is increased from $k\langle h_0\rangle=0.01$ (dark blue) to 0.04 (light blue). This insensitivity to $k\langle h_0\rangle$ occurs because the An spectrum is dominated by mode coupling [9,11]. During the reacceleration, the An spectrum grows more slowly because the longer wavelengths dominating the flow at this time are not seeded. For the aspect ratio in Fig. 3(c), all four cases generally agree with the experiments, but we show only one example for each spectrum for clarity. The only discrepancy occurs during the deceleration phase since the NS do not exhibit as much reduction in D_b/h_b as in the experiments.

The spikes are more difficult to calculate than bubbles, as shown in Fig. 4, because they have a smaller aspect ratio than bubbles even for $A=0.48$. As with the bubbles, the An spectrum underestimates the amplitude during the reacceleration even at the larger $k\langle h_0\rangle=0.04$. The Bb spectrum agrees well with the data up to $Z=35$ cm, but the subsequent evolution seems to need 512 zoning or better to match the data. The apsect ratio in Fig. 4(c) agrees with the data within the experimental variation. However, near the end, D_b/h_b is decreasing in the experiment while increasing slightly in the NS. These results suggest that the numerical dissipation (zoning) affects the spikes more than the bubbles since they are smaller in width for $A\geqslant0.5$, and better resolution is required to describe the spikes late in time.

To further justify our choice of initial spectra and amplitude in the NS, we compare them with experiments with a

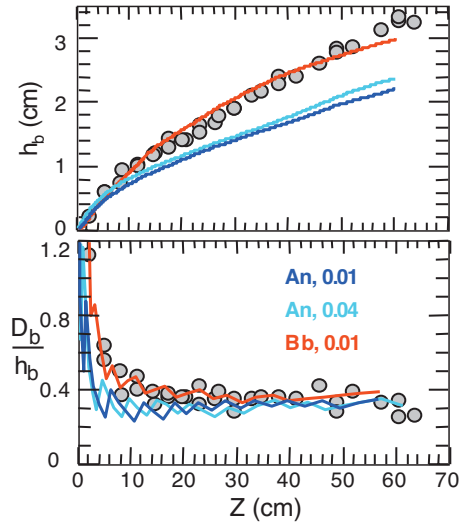

FIG. 5. (Color) Bubble amplitude and aspect ratio vs displacement for constant acceleration. Points are measured and lines are from NS with 256 zoning and different spectra and $\langle kh_0\rangle=0.01$.

constant $g\sim45g_0$, as shown in Fig. 5 for bubbles and Fig. 6 for spikes. These NS are performed with a zoning of $256\times256\times512$. As in Fig. 3, the amplitude growth and aspect ratio are large initially until the perturbations become nonlinear. Then, they grow self-similarly as successively longer wavelengths dominate the flow. The results with the Bb spectrum agree with the experiment with average values of $\alpha_b\sim0.048$ and $\alpha_s\sim0.06$. The An spectrum is unable to reproduce the data even by increasing $k\langle h_0\rangle$ because the long-wavelength modes dominating the late-time flow are not seeded. They must be generated by the mode-coupling

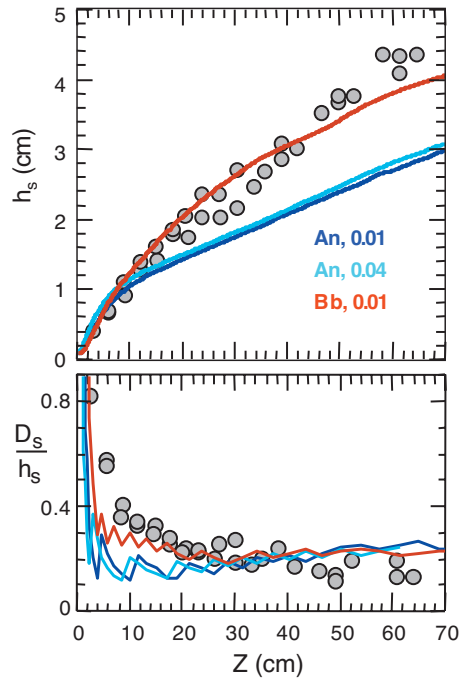

FIG. 6. (Color) Spike amplitude and aspect ratio vs displacement for constant acceleration. Points are measured and lines are from NS with 256 zoning and different spectra and $\langle kh_0\rangle=0.01$.

(merger) process, which is slower and yields $\alpha_b \sim 0.027$ and $\alpha_s \sim 0.031$. This again suggests that the initial perturbations in the LEM are more broadband than annular and the flow is dominated more by bubble competition than merger. It is interesting that both spectra are able to describe the self-similar aspect ratio $D_b/h_b \sim 0.35$ and $D_s/h_s \sim 0.2$. These values are in the middle of the range obtained on the LEM [7]—namely, $D_b/h_b \sim 0.28\ (1+A)$ and $D_s/h_s \sim 0.28\ (1-A)$. They are also consistent the aspect ratios calculated by Mikaelian [27] and Dimonte [14].

With this simpler acceleration, one can evaluate the physical validity of the value $k\langle h_0\rangle \sim 0.01$ chosen to fit the data in Figs. 3–6, since it exceeds the $k\langle h_0\rangle \sim 3\times 10^{-4}$ estimated from the initial experimental images [14]. This discrepancy may due to the fact that the short-wavelength modes that dominate the flow initially grow more slowly in the NS than in the experiments due to numerical viscosity [11] $\nu \sim 0.22\sqrt{Ag\Delta}$ (Δ=zone size). To quantify this effect, we note that the most unstable mode in the NS has [11] a wave number

$$k_0 \sim 0.5\left(\frac{Ag}{\nu^2}\right)^{1/3} \Rightarrow 48\ \frac{\text{rad}}{\text{cm}}. \tag{1}$$

The experiments are dominated by surface tension and have

$$k_0 \sim \sqrt{\frac{(\rho_H-\rho_L)g}{3\sigma}} \Rightarrow 47\ \frac{\text{rad}}{\text{cm}}. \tag{2}$$

The peak growth rate can then be written [11] as

$$\Gamma(k_0) \sim R_0\sqrt{Ak_0g}, \tag{3}$$

where the reduction factor is $R_0 \sim 0.65$ for viscosity and 0.82 for surface tension. The initial growth of the most unstable modes follows $\cosh(\Gamma t)$ until they become nonlinear [14] with $k\langle h\rangle \sim \sqrt{\pi}$. This occurs over a time

$$t_{NL} \sim \frac{1}{\Gamma(k_0)}\ln\left(\frac{2\sqrt{\pi}}{k_0\langle h_0\rangle}\right), \tag{4}$$

corresponding to a distance

$$Z_{NL} = \frac{1}{2}gt_{NL}^2 \sim \frac{1}{2AR_0^2k_0}\ln^2\left(\frac{2\sqrt{\pi}}{k_0\langle h_0\rangle}\right). \tag{5}$$

Z_{NL} can be identified in Figs. 3–6 as when the aspect ratio becomes constant (self-similar) and this occurs near $Z \sim 4$ cm. To obtain such a value with Eq. (5), $k\langle h_0\rangle$ needs to be of order 10^{-2} in the NS and 10^{-4} in the experiment because their values of R_0 are so different. This suggests that the larger initial amplitudes in the NS are required to compensate for the retarded growth initially due to numerical viscosity. However, further simulations and experiments are required to test this hypothesis.

The atomic mixing also depends on the acceleration history and the initial spectrum. This can be seen in Fig. 7 by plotting the calculated global atomic mix fraction [9,11–13]

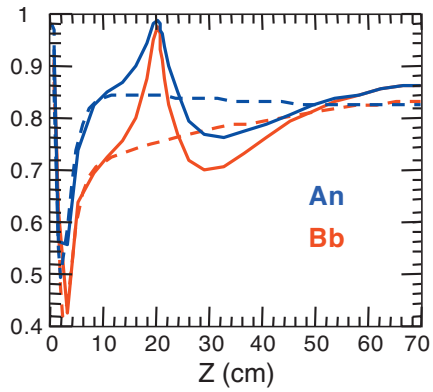

FIG. 7. (Color) Global mixing fraction vs displacement from NS with 256 zoning and $\langle kh_0\rangle$=0.01 for the An (blue) and Bb (red) spectra. Solid lines are for $g(t)$, and dashed lines are for constant g.

$$\Theta \equiv \frac{\int \langle f_H f_L\rangle dz}{\int \langle f_H\rangle\langle f_L\rangle dz} \tag{6}$$

for the NS with $k\langle h_0\rangle$=0.01. Angular brackets indicate averages in the transverse directions. For a constant g (dashed lines), the atomic mixing approaches the asymptotic value of $\Theta \sim 0.8$ at the same time that the flow becomes self-similar ($Z \sim 4$ cm). (The initial value near unity is an artifact of our initialization procedure.) The An spectrum exhibits more atomic mixing in the initial stage because there is more mode coupling. For the complex $g(t)$ (solid lines), the atomic mixing nearly complete ($\Theta \Rightarrow 1$) during the RT-stable stage. This is evident in the simulation images in Fig. 2(c) in which bubble and spike structures are replaced by horizontal bands of purely mixed fluids. Then, in the initial reacceleration, the atomic mixing falls below that observed for the constant g. This may contribute to the enhanced growth observed in Figs. 3 and 4 during this period.

IV. SUMMARY

We have performed experiments and NS on the RT instability with consecutive periods of RT-unstable, -stable, and -unstable acceleration. In the initial RT-unstable acceleration, the perturbations grow to a self-similar state on a time scale dependent on the initial perturbations. During the RT-stable deceleration, the amplitude and aspect ratio decrease as the dominant bubbles and spikes reverse their flow and become shredded by the trailing smaller-scale structures. This causes the fluids to become nearly completely mixed atomically. The instability recovers during the second unstable acceleration and approaches the asymptotic self-similar growth. The NS are in good agreement with the experiment only for the broadband initial perturbations. This suggests that the initial perturbations in the LEM experiment are more broadband than annular and the flow is dominated more by bubble competition than bubble merger. This suggests that the measured α_b should depend weakly on the initial amplitude [13,14].

This complex acceleration history reveals two important features that need to be described by mix models. First, the dominant bubbles and spikes at the front reverse their flow and become shredded during the RT-stable deceleration. This causes their diameter to decrease twofold and the atomic mixing to increase to 100%. As a result, the reduction in the mixing zone is only of order D_b. Second, the regrowth of the mixing zone during the second RT-unstable acceleration is delayed because of the high drag (small D_b) and atomic mixing. However, the mixing zone soon recovers and resumes the asymptotic growth. This recovery time will be a sensitive test for the mix models, which will be investigated in a subsequent publication.

ACKNOWLEDGMENTS

We would to like to thank David Youngs for motivating this work and for many fruitful discussions. This work was performed for the U.S. Department of Energy by Los Alamos National Laboratory under Contract No. DE-AC52-06NA25396.

[1] S. Atzeni and J. Meyer-Ter-Vehn, *The Physics of Inertial Fusion* (Clarendon Press, Oxford, 2004).
[2] V. N. Gamezo *et al.*, Science **299**, 77 (2003).
[3] Guy Dimonte and M. Schneider, Phys. Rev. E **54**, 3740 (1996).
[4] A. Llor, *Statistical Hydrodynamic Models for Developed Mixing Instability Flows* (Springer, Heidelberg, 2005).
[5] K. I. Read, Physica D **12**, 45 (1984).
[6] D. L. Youngs, Physica D **37**, 270 (1989).
[7] Guy Dimonte and M. Schneider, Phys. Fluids **12**, 304 (2000).
[8] P. Ramaprabhu and M. J. Andrews, J. Fluid Mech. **502**, 233 (2004).
[9] D. L. Youngs, Laser Part. Beams **12**, 725 (1994).
[10] D. Oron *et al.*, Phys. Plasmas **8**, 2883 (2001).
[11] Guy Dimonte *et al.*, Phys. Fluids **16**, 1668 (2004).
[12] W. H. Cabot and A. W. Cook, Nat. Phys. **2**, 562 (2006).
[13] P. Ramaprabhu, Guy Dimonte, and M. J. Andrews, J. Fluid Mech. **536**, 285 (2005).
[14] Guy Dimonte, Phys. Rev. E **69**, 056305 (2004).
[15] J. C. Hanson *et al.*, Laser Part. Beams **8**, 51 (1990).
[16] U. Alon, J. Hecht, D. Ofer, and D. Shvarts, Phys. Rev. Lett. **74**, 534 (1995).
[17] J. D. Ramshaw, Phys. Rev. E **58**, 5834 (1998).
[18] Guy Dimonte, Phys. Plasmas **7**, 2255 (2000).
[19] S. Gauthier and M. Bonnet, Phys. Fluids A **2**, 1685 (1990).
[20] Ye Zhou, G. B. Zimmerman, and E. W. Burke, Phys. Rev. E **65**, 056303 (2002).
[21] Guy Dimonte and R. Tipton, Phys. Fluids **18**, 085101 (2006).
[22] N. Freed *et al.*, Phys. Fluids A **3**, 91 (1991).
[23] A. J. Scannapieco and B. L. Cheng, Phys. Lett. A **299**, 49 (2002).
[24] S. G. Zaytsev *et al.*, Laser Part. Beams **21**, 393 (2003).
[25] Y. A. Kucherenko *et al.*, in *Proceedings of the Sixth International Workshop Physics Compressible Turbulent Mixing*, edited by G. Jourdan and L. Houas (Imprimerie Caractere, Marseille, 1997), p. 258.
[26] M. J. Andrews, Int. J. Numer. Methods Fluids **21**, 205 (1995).
[27] K. O. Mikaelian, Physica D **36**, 343 (1989).